Effect of Tempering Temperature on the Corrosion Behavior of R5 Steel in Artificial Seawater

Shiyang Zhang[1], Xiaoying Cheng[1,2,*] , Lingchao Su[1], Chaowei Jiang[1]

[1] Institute of Materials, Shanghai University, Shanghai 200072, China
[2] Laboratory for Microstructures, Shanghai University, Shanghai 200444, China
[*]E-mail: chengxyshu@126.com

The effect of tempering temperature (560 °C, 600 °C and 640 °C, denoted as T560, T600 and T640, respectively) on the corrosion behavior of R5 steel (a kind of mooring chain steel) in artificial seawater was studied by immersion tests and electrochemical measurements combined with scanning electron microscopy (SEM). X-ray diffraction (XRD) was conducted to analyze the corrosion products. The results indicated that the corrosion resistance of the steel was increased with elevating tempering temperature. Steel T640 with higher tempering temperature exhibited excellent corrosion resistance with lower corrosion current density, a less weight loss and bigger impedance modulus than steels T560 and T600. The distinction of corrosion resistance can be attributed to the different grain size and carbide density in the microstructure.

1. INTRODUCTION

Nowadays, the exploitation and utilization of marine resources have become a hot point all over the world, which provide a tremendously high marketing demand for the mooring chain steel. Offshore platforms have offered an effective solution for oil-gas discovery in deep-sea. They are tied up to the seabed through mooring systems, which are composed of anchor systems, connectors, and chains. Due to the poor conditions of service, mooring chains are required to withstand long-term continuous wave buffeting and the erosion of seawater. A large number of chloride ions in seawater accelerate the corrosion of the mooring chain steel. Because chloride ions can penetrate through the corrosion films, particularly via flaws and defects, then further reach the metal base [1]. Therefore, to

make sure the safety of offshore platforms, the mooring chain steel requires not only high strength but also excellent corrosion resistance of seawater.

Mooring chain steel is a kind of high strength low alloy (HSLA) steel. The research about corrosion behavior and mechanism of HSLA steel has been carried out for many years. It has reported that low alloy steel after heat treatment displays excellent mechanical properties, with good ductility and high tensile strength [2-4]. Heat treatment is also an effective way to improve the corrosion resistance of steels [5-8]. Guo et al. [9] reported the microstructure of a low alloy steel under different cooling rates. The steel with acicular ferrite microstructure exhibited outstanding corrosion resistance. It was proved that the corrosion behavior of an IF (interstitial-free) steel was intimately associated with resulting microstructure. Due to pearlite absence, its corrosion potential indicated better corrosion resistance when compared with conventional low and ultra-low carbon steels [10]. Additionally, a dual-phase steel produced under intercritical annealing evidenced slightly smaller corrosion resistance when compared with other treated low carbon steels [11]. This was attributed to distorted microstructure provided by a residual stress when the martensite was constituted [11]. This clearly demonstrated the interrelation of the resulting microstructure arrays provided of different steels by distinctive treatments on the corrosion behavior. Lu et al. [12] investigated the corrosion resistance of a martensitic stainless steel that was tempered at 300 °C, 500 °C and 650 °C, separately. While tempered at 500 °C, the corrosion resistance of the steel reduced suddenly. The consequences indicated that pitting started at substantial interfaces of carbide/matrix, which were provided by the massive amount of precipitated nanoscale chromium-rich $M_{23}C_6$ carbides. The small gap between the tempering carbides would impede the generation of a protective passive film on the steel matrix. Zhou et al. [13] reported the corrosion behavior of low carbon micro alloyed steel in a Cl^- containing environment. The corrosion processes were divided into the initial stage and the later stage. The rust layers of the test steels were found to be composed of Fe_3O_4, α-FeOOH, β-FeOOH, γ-FeOOH and large amounts of amorphous compounds.

In our previous work [14], we researched the effect of tempering temperature on the mechanical properties and microstructure of the mooring chain steel, but the effect on the corrosion behavior was not studied. The aim of this paper was to evaluate the influence of tempering temperature on the corrosion behavior of the mooring chain steel in artificial seawater. The corrosion resistance of the steel was characterized by weight loss measurements, electrochemical impedance spectroscopy (EIS) measurements and potentiodynamic polarization tests. The corrosion products were analyzed by X-ray diffraction (XRD). Besides, corrosion surface morphologies of these specimens were observed by scanning electron microscopy (SEM).

2. EXPERIMENTAL

2.1 Materials and heat treatment

The original R5 steel used in this study was a mooring chain steel provided by Jiangsu Asian Star Anchor Chain Co. Ltd. Table 1 shows the chemical composition of the steel. The following heat

treatment was carried out in our laboratory. After austenization at 920 °C for 30 min, samples were quenched in ice-water and then tempered at 200 °C for 3 h to release residual stress. Next, the treated steel was cut into several designed specimens and these specimens were tempered at higher temperature (560 °C ± 2 °C, 600 °C ± 2 °C and 640 °C ± 2 °C) for 3h to obtain different tempered microstructures, corresponding to specimen codes T560, T600 and T640, separately.

The samples prepared for immersion tests had a dimension of 20 mm × 20 mm × 2 mm, whereas those for the electrochemical tests were 10 mm × 10 mm × 5 mm. Artificial seawater was used as the test medium, composed of (per liter of distilled water): 27 g NaCl, 6 g $MgCl_2$, 1 g $CaCl_2$, 1 g KCl. The solution was stirred evenly.

Table 1. Chemical composition of the investigated steel (wt.%)

C	Mn	Cr	Ni	Mo	Si	Al	V	Fe
0.22	0.65	2.05	1.20	0.46	0.30	0.02	0.05	Bal.

2.2 Immersion test

All the samples were polished with a series of SiC emery papers with 200-grit to 1200-grit, then cleaned with acetone and ethanol ultrasonic and dried by air. After measuring the initial mass, the specimens were immersed in artificial seawater for 360 hours. After the test, all the samples were cleaned with distilled water, then pickled in a solution of 500 ml HCl + 3.5 g hexamethylene tetramine + balanced distilled water for 10 min to eliminate the corrosion products. After the products were totally removed, the samples were carefully cleaned with acetone and ethanol ultrasonic, then dried in air. The final mass of the test sample was measured for the weight loss test.

2.3 Electrochemical measurements

The exposed surface of the samples for electrochemical measurements was 10 mm × 10 mm, with an area of 1 cm^2. All of the electrochemical test samples were enclosed with epoxy resin, leaving a working area of 1 cm^2. Before testing, the exposed surface was ground with 200-grit to 1200-grit SiC papers and cleaned with acetone and ethanol ultrasonic, then dried in air. All electrochemical experiments were performed using an electrochemical workstation CS350, manufactured by Wuhan CorrTest Instruments Co., China. A three-electrode system was applied in the potentiodynamic polarization tests and electrochemical impedance spectroscopy tests, with the steel specimen as the working electrode (WE), a platinum sheet as the counter electrode (CE) and a saturated calomel electrode (SCE) as the reference electrode (RE). All the potentials reported here were measured relative to the value of SCE. The test temperature was controlled at 30 °C by an electro-thermostatic water bath. The open circuit potentials (OCPs) of all WEs were monitored for 1 h until stable OCPs were achieved. Then, the EIS measurements were performed firstly with a 10 mV amplitude perturbation and a frequency range from 100 kHz to 0.01 Hz. The experimental results were

fitted and analyzed by ZSimpWin. Potentiodynamic polarization test was conducted vs. open circuit potential from −0.2 V to 0.2 V at a scan rate of 0.5 mV/s. The fitting parameters were determined from the polarization curves using the CView software. The electrochemical results of each type of specimens were averaged based on at least Three parallel samples from the same heat treatment.

2.4 Analysis of corrosion products by SEM and XRD

The corroded surfaces of the samples were observed by scanning electron microscope of HITACHI SU-1500 type. The components of corrosion products were examined by a D/MAX2200V X-ray diffractometer with a Cu target. The scan speed was 2°/min and the 2θ angle ranged from 10° to 90°. Further analyses of XRD spectra were carried out with Jade 6.5 software program.

3. RESULTS AND DISCUSSION

3.1 Potentiodynamic polarization curves

Potentiodynamic polarization was measured on the samples with a fresh surface after 1 h immersion and 360 h immersion. The polarization curves of the specimens measured in artificial seawater are shown in Fig. 1. As can be seen, the anodic current densities increase continuously with increasing corrosion potentials, which indicate all specimens show active dissolution behaviors without passivation [15]. The anodic and cathodic branches show Tafel behavior. Therefore, Tafel extrapolation can be used to calculate the corrosion kinetics parameters.

The values of electrochemical parameters derived from the polarization curves are given in Table 2. All these polarization curves have similar shapes in anodic and cathodic branches. The anodic and cathodic Tafel constants (b_a, b_c, respectively) do not change significantly for samples, which indicate the analogous mechanism for the corrosion reaction of these steels in artificial seawater. For bare steel, the corrosion current density (i_{corr}) decreases with increasing tempering temperature, while the corrosion potential (E_{corr}) shifts towards the noble direction. It reveals the corrosion resistance of the test steels has become better and better.

After 360 h immersion, the corrosion potentials (E_{corr}) all shift to a positive value. Compared with the bare steels, the corrosion current densities of the samples after 360 h immersion are smaller, which demonstrate that the corrosion films have a certain protective effect. Moreover, the corrosion rates of the three tempered steels immersed for 360 h were calculated from the corrosion current densities taken from Tafel plot by Faraday's law [16]:

$$V = 0.00327(ai/nD) \tag{1}$$

Where V is the corrosion rate (mm/year), a is the molar mass of studied steel (g/mol), i is corrosion current density ($\mu A/cm^2$), n is valency, D is steel density (g/cm^3). Steel T640 has lower corrosion rate than steels T560 and T600, which demonstrates the corrosion resistance of steel T640 is higher than other steels.
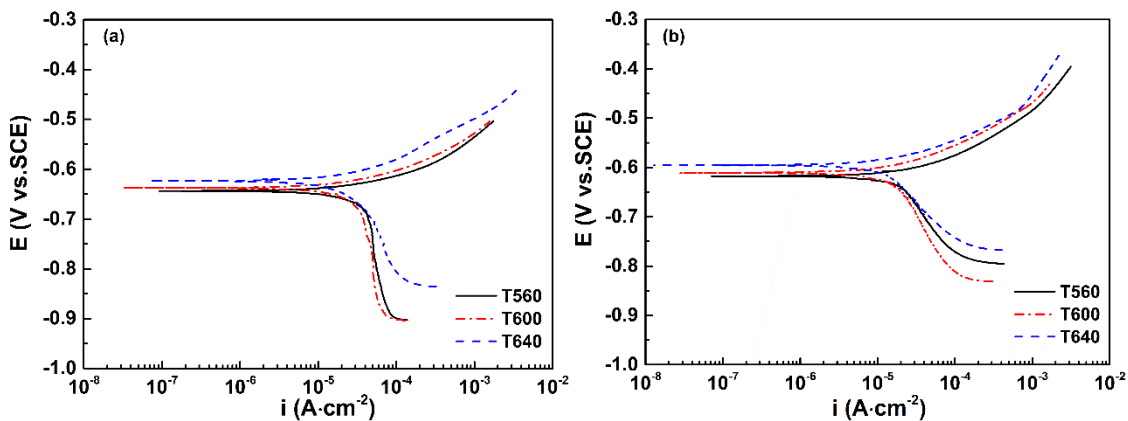
Figure 1. Potentiodynamic polarization curves of the specimens in artificial seawater: (a) bare steels, (b) steels after 360 h immersion

Table 2. Potentiodynamic polarization parameters from a curve-fitting approach

Type	Specimen	E_{corr} (V)	i_{corr} ($\times 10^{-6}$A/cm^2)	b_a (V/decade)	b_c (V/decade)
	T560	-0.6438	59.153	0.086	-0.298
Bare steel	T600	-0.6374	49.016	0.081	-0.312
	T640	-0.6238	37.140	0.087	-0.334
	T560	-0.6177	44.390	0.084	-0.254
Steel after 360 h immersion	T600	-0.6112	27.132	0.088	-0.263
	T640	-0.5953	19.320	0.077	-0.278
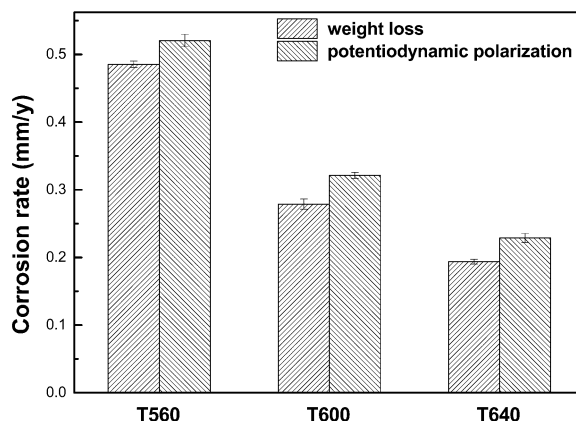
Figure 2. Comparison of corrosion rates between potentiodynamic polarization and weight loss measurements after 360 h immersion

Fig. 2 shows that the tendency of the corrosion rate is also in good accordance with weight loss method. The average corrosion rates from the immersion tests were calculated by the following equation [17]:

$$V = 87600 \Delta m / s\rho t \qquad (2)$$

The specimen is the rectangular shape for $20mm \times 20mm \times 2mm$, where *V* is the corrosion rate (mm/year), Δm is the weight change after the corrosion test (g), *s* is the surface area of the specimen (cm^2), ρ is the density of the test steel (g/cm^3), *t* is the immersion time (h).

3.2 Electrochemical impedance spectroscopy (EIS)

To confirm the results of the potentiodynamic polarization, the electrochemical impedance spectroscopy (EIS) measurements were performed under the same experimental conditions as the polarization curves. Fig. 3 exhibits the Nyquist plots of bare steels in artificial seawater. It can be seen that each spectrum includes a single semicircle. The diameter of the semicircle increases with elevating tempering temperature, which implies that the corrosion resistance of steel T640 is the best among these steels.
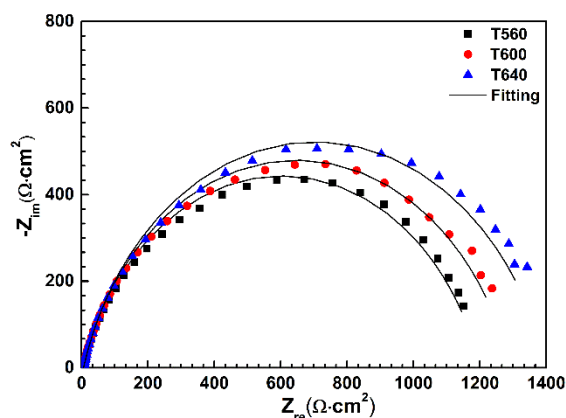

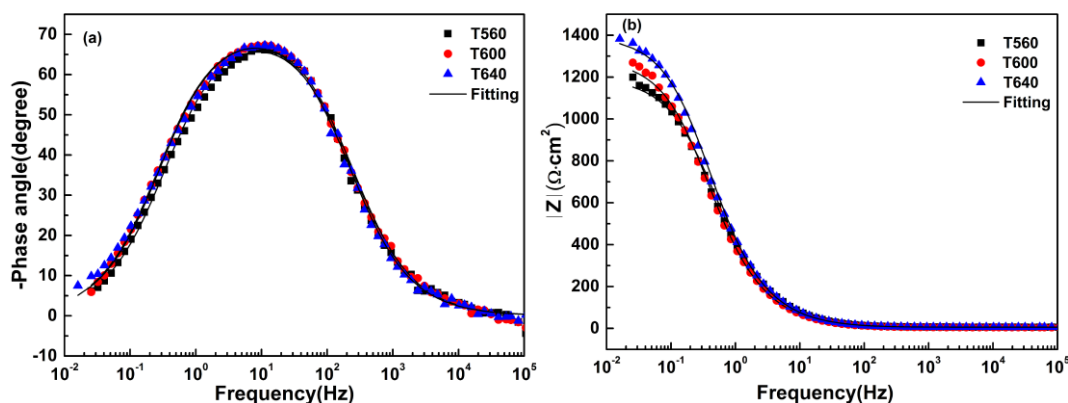**Figure 3.** Nyquist plots of bare steels in artificial seawater

Figure 4. Bode diagrams of bare steels in artificial seawater: (a) the phase-frequency characteristic curve, (b) the amplitude-frequency characteristic curve

Fig. 4 shows the Bode diagrams of bare steels in artificial seawater. From Fig. 4(b), the impedance modulus |Z| of experimental steels gradually increases with elevating tempering temperature in the low-frequency range, and the impedance modulus |Z| is biggest for steel T640, while

the smallest one is for steel T560. The corrosion rate is highest for steel T560 and lowest for steel T640, because the impedance modulus in the low-frequency range is inversely proportional to the corrosion rate of the steel [18]. The number of time constants can be used to determine the number of state variables included in the surface reactions of the electrode process [19]. Only one time constant can be obtained from Fig. 4(a). The spectra of all specimens show a single capacitive in the high-medium frequency range, which are in relation to the double layer capacitance in parallel with the charge transfer resistance [20].
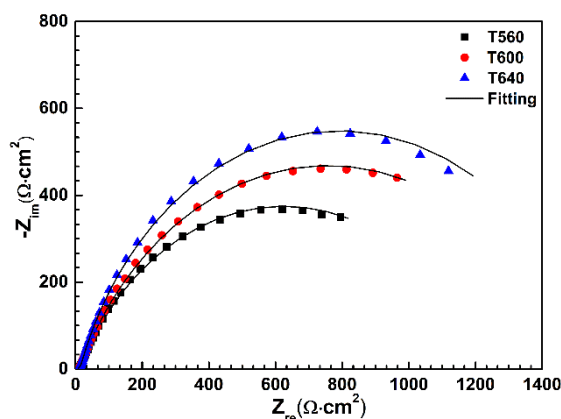

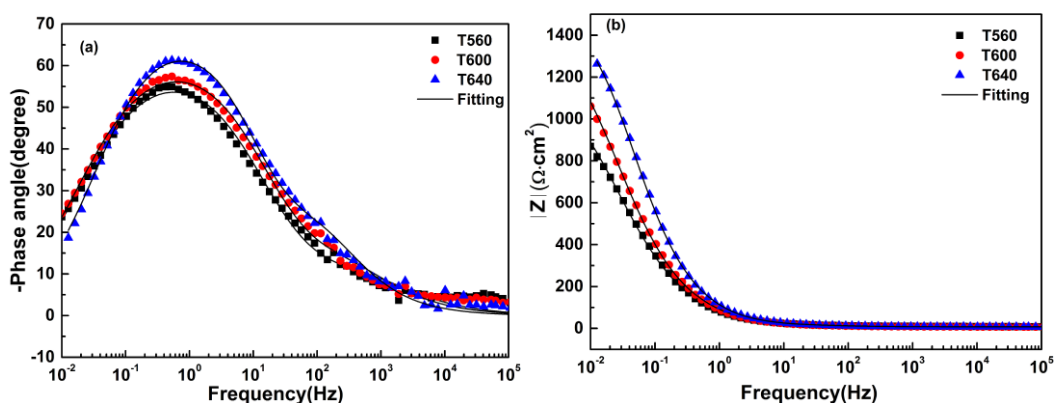**Figure 5.** Nyquist plots of the specimens in artificial seawater after 360 h immersion

Figure 6. Bode diagrams of the specimens in artificial seawater after 360 h immersion: (a) the phase-frequency characteristic curve, (b) the amplitude-frequency characteristic curve

For a better understanding of the corrosion process, the Nyquist plots and Bode diagrams of the test steels after 360 h immersion are displayed in Fig. 5 and Fig. 6 respectively. From Fig. 5, it is apparently found that the semicircle diameter of the experimental steel become larger with elevating tempering temperature, which implies the improvement of corrosion resistance for tested steels. Fig. 6(a) shows two-time constant behavior. In general, the time constant at high frequencies could be correlated with the electronic properties of the corrosion film, while the time constant at intermediate frequencies is associated with the charge transfer process at the film/solution interface [19, 21]. Besides, the maximum magnitude of phase angle shifts towards low-frequency range when immersed for 360 h. The reason could be attributed to the formation of corrosion films on the surface of steels

[22]. Fig. 6(b) shows that the impedance modulus |Z| in low-frequency range gradually increases with elevating tempering temperature, which reveals that the corrosion resistance of steel T640 is much better than other steels.

Based on above impedance spectra features, the electrochemical behavior can be simulated by equivalent circuits of Fig. 7. The ZSimpWin software was applied to fit the EIS data. Fig. 7(a) was simulated to the impedance spectra with one time constant and Fig. 7(b) was fitted to the impedance spectra with two time constants. The fitting results are presented in Table 3. In these models, R_{ct} is the charge transfer resistance associated with the difficulty of the electrochemical reaction. R_s is the resistance of solution. R_f is the resistance of corrosion film. Q_f and Q_{dl} are the CPE parameters for film and double layer of film-electrolyte interface respectively. CPE is the constant phase element, which is generally used in place of a capacitance to explain the non-ideal capacitance response due to the nearly complete absence of pure capacitance in the actual electrochemical process [23, 24]. The impedance of a constant phase element is defined as $Z_{CPE} = [Q(j\omega)^n]^{-1}$, where Q is a proportional factor, j is the complex operator with $j = (-1)^{1/2}$, $\omega = 2\pi f$ is the angular frequency, n is an exponential term. If $n = 0$, the impedance is ideal resistance, while it is ideal capacitance if $n = 1$. And $0 < n < 1$ represents the deviation from the ideal capacitance, which is correlated with the surface roughness and defect [15, 25]. The equivalent impedance Z, shown in Fig. 7(a) can be expressed as:

$$Z = R_s + \frac{1}{\frac{1}{Z_{Q_{dl}}} + \frac{1}{R_{ct}}} \qquad (3)$$

The equivalent impedance Z, shown in Fig. 7(b) can be written as:

$$Z = R_s + \frac{1}{\frac{1}{Z_{Q_f}} + \frac{1}{R_f + \frac{1}{\frac{1}{Z_{Q_{dl}}} + \frac{1}{R_{ct}}}}} \qquad (4)$$

As shown in Table 3, R_s is quite low and changes little, due to the good conductivity of the solution and the relative stability of the test system. It is well known that the polarization resistance (R_p) is inversely proportional to the corrosion rate [26, 27]. In the initial stage, the corrosion procedure of the steels is totally controlled by the charge transfer resistance (R_{ct}). The total polarization resistance (R_p) is equal to R_{ct}. After 360 h immersion, since the formation of corrosion films, R_p is equal to the sum of R_{ct} and R_f, which has been widely used to explain the kinetics of electrochemical corrosion[28]. For bare steels, the R_p value of steel T640 is larger than other steels, which shows steel T640 has the best corrosion resistance among these steels. Furthermore, values of R_p increase after 360 h immersion for all the samples, which could be ascribed to the protective corrosion products formed on the surface of the steel. These results are in agreement with those obtained from potentiodynamic polarization measurement.
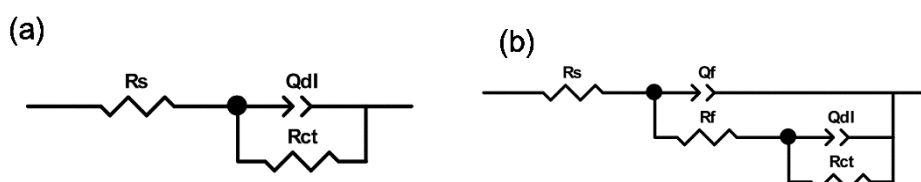

Figure 7. Equivalent circuits for EIS data fitting

Table 3 . The parameters of equivalent circuits for steels

Type	Specimen	R_s (Ω cm^2)	Q_{dl} (Ω^{-1} cm^2 s^n)	n_{dl}	R_{ct} (Ω cm^2)	Q_f (Ω^{-1} cm^2 s^n)	n_f	R_f (Ω cm^2)	R_p (Ω cm^2)
Bare steel	T560	5.78	0.0004543	0.8127	1195				1195.00
	T600	4.99	0.0005047	0.8157	1287				1287.00
	T640	5.93	0.0004496	0.8175	1396				1396.00
Steel after 360 h immersion	T560	8.23	0.0023340	0.7210	1226	0.001160	0.6549	6.63	1232.63
	T600	7.50	0.0017300	0.7424	1490	0.001304	0.6787	8.44	1498.44
	T640	7.74	0.0011190	0.8155	1550	0.001036	0.7453	16.65	1566.65

3.3 Analysis of corrosion products

Fig. 8 shows the SEM morphologies of the outer layer of the corroded surfaces after 360 h immersion in artificial seawater. The corrosion products of steel T560 are porous, defective and loose, which look like flocs and spherical clusters, as shown in Fig. 8(a). Pores and cracks existing among these corrosion products can visibly provide transmission channels for corrosion medium, such as moisture and oxygen [13], which will promote the corrosion process. With increasing tempering temperature, the outer rust layer structure of each specimen changes from loose to compact. It is evident that the surface of steel T640 is the most homogeneous and compact of the three-group tested steels, as shown in Fig. 8(c). The specimen surface is covered uniformly by corrosion products, and granules of corrosion products are much smaller.
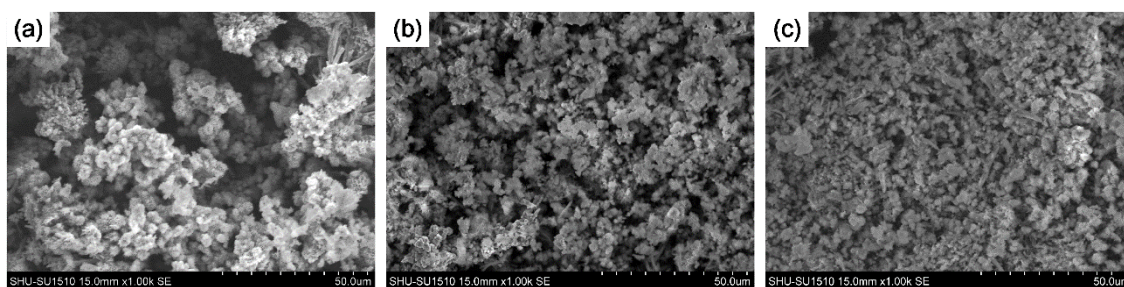

Figure 8. SEM morphologies of the outer layer of the corroded surfaces after 360 h immersion in artificial seawater: (a) steel T560; (b) steel T600; (c) steel T640

Fig. 9 shows the SEM morphologies of the inner layer of the corroded surfaces after 360 h immersion in artificial seawater. The corrosion products of the outer layer were easily removed with a soft brush, which had limited protection to the steel substrate. Compared to the outer rust layer, the inner rust layer was compact and adherent to the steel, which was difficult to wipe off by physical methods. Thus it showed good protection to the substrate. As we can see, there are still some cracks on the inner surface, especially on steel T560. With the increase of tempering temperature, the dense cracks gradually decrease, and the rusts become uniform, which can effectively protect the substrate out of corrosion mediums, so as to slow down the corrosion rate.
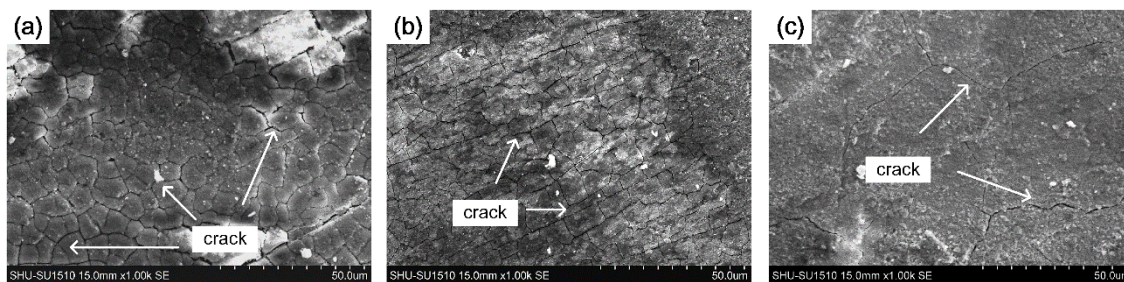
Figure 9. SEM morphologies of the inner layer of the corroded surfaces after 360 h immersion in artificial seawater: (a) steel T560; (b) steel T600; (c) steel T640

Fig. 10 shows the SEM morphologies of the steels immersed for 360 h after corrosion products removal. As shown in Fig. 10(a), there are many pitting holes on the surface of steel T560. With elevating tempering temperature, the number of corrosion pits reduces. The surface of steel T640 shown in Fig. 10(c) is relatively better than the samples in Fig. 10(a) and Fig. 10(b). Apparently, the corrosion degree decreases with the increased tempering temperature.
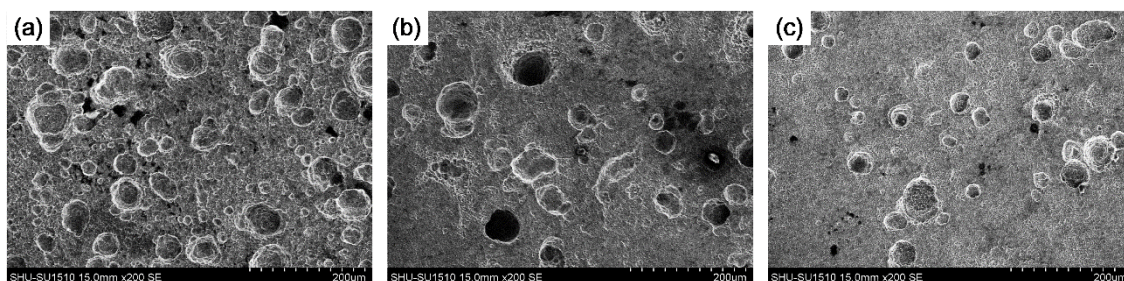

Figure 10. SEM morphologies of the steels immersed for 360 h after corrosion products removal: (a) steel T560; (b) steel T600; (c) steel T640

The compositions of corrosion products on the three tempered steels were determined by XRD analysis, as shown in Fig. 11. It can be obtained that the corrosion products of all samples are composed of the same compositions in artificial seawater, mainly including γ-FeOOH and Fe_3O_4. The results are similar to those reported for the corrosion products of low alloy steel in conditions containing chloride ions [9, 29, 30]. The corrosion of steel is known to be an electrochemical process. The formation process of the corrosion products on the steel could be discussed in the followings [31]:

Anodic: $Fe \rightarrow Fe^{2+} + 2e^-$ (5)
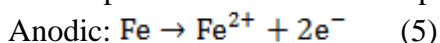
In seawater, adsorption of the chloride ions to the surface led to the formation of soluble metal–chloride complexes [32]:
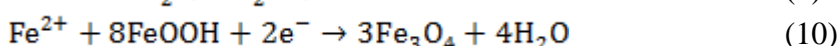
$$Fe^{2+} + 2Cl^- + 4H_2O \rightarrow FeCl_2 \cdot 4H_2O \quad (6)$$

$$FeCl_2 \cdot 4H_2O \rightarrow Fe(OH)_2 + 2Cl^- + 2H^+ + 2H_2O \quad (7)$$

$$4Fe(OH)^+ + 4OH^- + O_2 \rightarrow 4FeOOH + 2H_2O \quad (8)$$

Cathodic: $O_2 + 2H_2O + 4e^- \rightarrow 4OH^-$ (9)

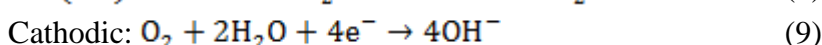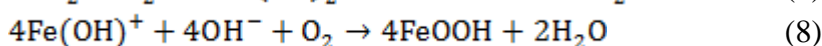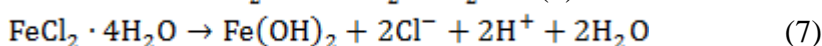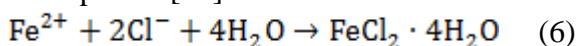$$Fe^{2+} + 8FeOOH + 2e^- \rightarrow 3Fe_3O_4 + 4H_2O \quad (10)$$

Table 4 displays the results of quantitative analysis of crystal phases in corrosion products. It can be found that the ratio of Fe_3O_4 decreases with elevating tempering temperature. During the process of corrosion, Fe_3O_4 with high electrical conductivity could be served as the cathode and increased the surface area of the cathode [33]. That would accelerate the corrosion rate of the steel matrix.

Table 4 . Quantitative analysis of crystal phases in corrosion products

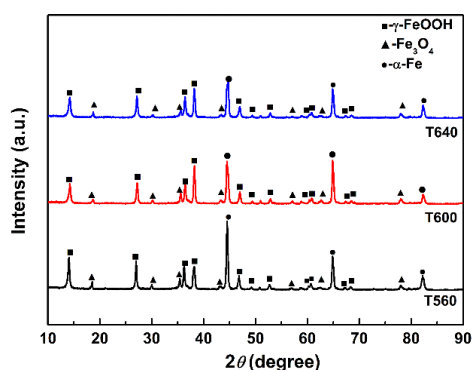| Specimen	α-Fe	γ-FeOOH	Fe_3O_4
T560	54.5 %	37.8 %	7.7 %
T600	53.4 %	40.0 %	6.6 %
T640	52.8 %	42.1 %	5.1 %

Figure 11. X-ray diffraction measurement of the three tempered samples after 360 h immersion in artificial seawater

3.4 Discussion

In the previous research of our group, the detailed microstructures of the three tempered steels were studied by transmission electron microscopy (TEM) and electron back-scattered diffraction (EBSD). The figures were shown in our previous paper [14]. It was obtained from EBSD analyses that the average grain sizes of steel T560, T600, and T640 were 0.13 μm, 0.15 μm, and 0.39 μm, respectively. Apparently, with increasing tempering temperature, the average grain sizes of the three tempered steels increased, while the grain boundary area decreased. It is well recognized that the grain boundaries are preferred corrosion sites in corrosion medium. Since the large density of crystal defects, and lattice distortion in the grain boundary, atoms have high energies, and become more active, will take part in the reaction first. As a result, the larger the volume fraction of grain boundaries, the more the active atoms on the steel surface, which lead to the increasing of anodic current density [34]. In addition, the formation of the galvanic couple between relatively anodic grain boundary and cathodic grain interior can also increase the corrosion rate [35]. Zhang et al. [36] reported WC-CO alloys with larger WC grain sizes exhibited better corrosion resistance in the solution of H_2SO_4. Ghosh D et al.

[37] found that the higher corrosion rate of fine grained steel was mainly due to higher grain boundary area, resulting in pronounced grain boundary attack due to oxidation/sulfidation along the grain boundaries. In conclusion, with the increase of tempering temperature, the grain boundary area decreased, which indicated the active sites for corrosion attack reduced, then the corrosion resistance of the tempered steels became better.

The results of TEM images [14] indicated that steel T560 had acicular ferrite with a high dislocation density. The density of dislocation and defect decreased considerably with the increase of tempering temperature. Carbides precipitated in Steel T560 were fine needle shape and dispersively distributed in the steel substrate. As the tempering temperature increased from 600 °C to 640 °C, carbides changed from sparse elliptical shape to spherical shape, the density of carbides decreased, and the interfaces between carbides and the matrix also decreased. From the diffractions, these carbides were assured to be Fe_3C. Many reports [22, 38, 39] have shown that Fe_3C provided an available area for the cathodic reactions. It could serve as the cathode in micro-electrochemical cells because of its more positive potential than ferrite. Accordingly, the ferrite matrix would act as the anode. Thus, the microcells would accelerate the corrosion of the ferrite, resulting in a higher corrosion rate (low charge-transfer resistance). It is suggested that dislocations are also the regions of preferential corrosion sites in seawater. With increasing tempering temperature, the quenching stress released thoroughly, and the density of dislocation decreased, then the microstructure became uniform and stable. As a result, the corrosion resistance of steels would be improved correspondingly.

4. CONCLUSIONS

The results obtained from the study of the effect of tempering temperature on the corrosion behavior of a mooring chain steel in artificial seawater have been presented. The following conclusions can be drawn from this investigation:

(1) Steel T640 with higher tempering temperature exhibited excellent corrosion resistance with lower corrosion current density , a less weight loss and bigger impedance modulus than steels T560 and T600.

(2) The corrosion products of the three tempered steels were all found to be composed of Fe_3O_4 and γ-FeOOH. With elevating tempering temperature, the outer rust layers became homogeneous, while the cracks in the inner rust layers decreased.

(3) The tempering temperature had a strong effect on the microstructure and corrosion resistance of the mooring chain steel. With elevating tempering temperature, the grain boundary area decreased, which indicated the active sites for corrosion attack reduced, then the corrosion resistance of the tempered steels became better. Moreover, the density of carbides decreased. So the microcells between carbides and the ferrite matrix reduced. As a result, the corrosion resistance of steels would be improved correspondingly.

References

1. M. Deyab, S.A. El-Rehim, *Electrochim. Acta.*, 53 (2007) 1754.
2. N. Zhong, X. Wang, L. Wang, Y. Rong, *Mater. Sci. Eng., A*, 506 (2009) 111.
3. A. Odeshi, M. Bassim, S. Al-Ameeri, *Mater. Sci. Eng., A*, 419 (2006) 69.
4. W. Zhou, V. Challa, H. Guo, C. Shang, R. Misra, *Mater. Sci. Eng., A*, 620 (2015) 454.
5. E. Atık, U. Yunker, C. Meriç, *Tribol. Int.*, 36 (2003) 155.
6. A. Candelaria, C. Pinedo, *J. Mater. Sci. Lett.*, 22 (2003) 1151.
7. S.-Y. Lu, K.-F. Yao, Y.-B. Chen, M.-H. Wang, X.-Y. Ge, *Metall. Trans. A*, 46 (2015) 6090.
8. A. Dugstad, H. Hemmer, M. Seiersten, *Corrosion*, 57 (2001) 369.
9. Y.-b. Guo, C. Li, Y.-c. Liu, L.-m. Yu, Z.-q. Ma, C.-x. Liu, H.-j. Li, *Int. J. Miner. Metall. Mater.*, 22 (2015) 604.
10. W. Osorio, L. Peixoto, A. Garcia, *Mater. Corros.*, 61 (2010) 407.
11. W. Osorio, L. Peixoto, L.R. Garcia, A. Garcia, *Mater. Corros.*, 60 (2009) 804.
12. S.-Y. Lu, K.-F. Yao, Y.-B. Chen, M.-H. Wang, X. Liu, X. Ge, *Electrochim. Acta.*, 165 (2015) 45.
13. Y. Zhou, J. Chen, Y. Xu, Z. Liu, Effects of Cr, *J. Mater. Sci. Technol.*, 29 (2013) 168.
14. X. Cheng, H. Zhang, H. Li, H. Shen, *Mater. Sci. Eng., A*, 636 (2015) 164.
15. W. Liu, Q. Zhou, L. Li, Z. Wu, F. Cao, Z. Gao, *J. Alloy. Compd.*, 598 (2014) 198.
16. C. Yu, X. Gao, P. Wang, *Electrochemistry*, 83 (2015) 406.
17. Q. Xu, K. Gao, W. Lv, X. Pang, *Corros. Sci.*, 102 (2016) 114.
18. B. He, C.-h. Lu, P.-j. Han, X.-h. Bai, *Eng Fail Anal*, 59 (2016) 410.
19. Q. Xie, W. Chen, *Corros. Sci.*, 86 (2014) 252.
20. S. Marcelin, N. Pébère, S. Régnier, *Electrochim. Acta.*, 87 (2013) 32.
21. H. Luo, C. Dong, X. Li, K. Xiao, *Electrochim. Acta.*, 64 (2012) 211.
22. W. Liu, H. Zhang, Z. Qu, Y. Zhang, J. Li, *J. Solid State Electrochem.*, 14 (2010) 965.
23. M. Lebrini, M. Lagrenée, H. Vezin, M. Traisnel, F. Bentiss, *Corros. Sci.*, 49 (2007) 2254.
24. Q. Qu, Y. He, L. Wang, H. Xu, L. Li, Y. Chen, Z. Ding, *Corros. Sci.*, 91 (2015) 321.
25. S.K. Kim, I.J. Park, D.Y. Lee, J.G. Kim, *J. Appl. Electrochem.*, 43 (2013) 507.
26. Y. Kayali, B. Anaturk, *Mater. Des.*, 46 (2013) 776.
27. H. Wang, P. Zhou, S. Huang, C. Yu, *Int. J. Electrochem. Sci.*, 11 (2016) 1293.
28. Z. Ai, J. Jiang, W. Sun, D. Song, H. Ma, J. Zhang, D. Wang, *Appl. Surf. Sci.*, 389 (2016) 1126.
29. H. Tamura, *Corros. Sci.*, 50 (2008) 1872.
30. Y. Lu, J. Dong, W. Ke, *J. Mater. Sci. Technol.*, 32 (2016) 341.
31. Y. Zou, J. Wang, Y. Zheng, *Corros. Sci.*, 53 (2011) 208.
32. M. Alizadeh, S. Bordbar, *Corros. Sci.*, 70 (2013) 170.
33. U. Evans, C. Taylor, *Corros. Sci.*, 12 (1972) 227.
34. Y. Li, F. Wang, G. Liu, *Corrosion*, 60 (2004) 891.
35. G. Argade, S. Panigrahi, R. Mishra, *Corros. Sci.*, 58 (2012) 145.
36. L. Zhang, Y. Chen, Q.-l. Wan, T. Liu, J.-f. Zhu, W. Tian, *Int. J. Refract. Met. Hard Mater.*, 57 (2016) 70.
37. D. Ghosh, S. Mitra, *High Temp. Mat. Pr-Isr.*, 31 (2012) 727.
38. J. Mora-Mendoza, S. Turgoose, *Corros. Sci.*, 44 (2002) 1223.
39. J. Sun, G. Zhang, W. Liu, M. Lu, *Corros. Sci.*, 57 (2012) 131.